RESEARCH ARTICLE

Upconversion nanoparticles for super-resolution quantification of single small extracellular vesicles

Guan Huang[1†], Yongtao Liu[1,2†], Dejiang Wang[1], Ying Zhu[1,3,4], Shihui Wen[1], Juanfang Ruan[5] and Dayong Jin[1,6,7*]

Abstract

Although small EVs (sEVs) have been used widely as biomarkers in disease diagnosis, their heterogeneity at single EV level has rarely been revealed. This is because high-resolution characterization of sEV presents a major challenge, as their sizes are below the optical diffraction limit. Here, we report that upconversion nanoparticles (UCNPs) can be used for super-resolution profiling the molecular heterogeneity of sEVs. We show that Er^{3+}-doped UCNPs has better brightness and Tm^{3+}-doped UCNPs resulting in better resolution beyond diffraction limit. Through an orthogonal experimental design, the specific targeting of UCNPs to the tumour epitope on single EV has been cross validated, resulting in the Pearson's R-value of 0.83 for large EVs and ~65% co-localization double-positive spots for sEVs. Furthermore, super-resolution nanoscopy can distinguish adjacent UCNPs on single sEV with a resolution of as high as 41.9 nm. When decreasing the size of UCNPs from 40 to 27 nm and 18 nm, we observed that the maximum UCNPs number on single sEV increased from 3 to 9 and 21, respectively. This work suggests the great potentials of UCNPs approach "digitally" quantify the surface antigens on single EVs, therefore providing a solution to monitor the EV heterogeneity changes along with the tumour progression progress.

Keywords Extracellular vesicles, Upconversion nanoparticles, Super-resolution, Liquid biopsy

[†]Guan Huang and Yongtao Liu contributed equally to this work

*Correspondence:
Dayong Jin
dayong.jin@uts.edu.au
[1] Institute for Biomedical Materials and Devices (IBMD), Faculty of Science, University of Technology Sydney, Sydney, NSW 2007, Australia
[2] Smart Computational Imaging Laboratory (SCILab), School of Electronic and Optical Engineering, Nanjing University of Science and Technology, Nanjing, Jiangsu 210094, China
[3] School of Biomedical Engineering, Faculty of Engineering and Information Technology, University of Technology Sydney, Sydney, NSW 2007, Australia
[4] School of Clinical Medicine, Faculty of Medicine & Health, UNSW Sydney, Sydney, NSW 2052, Australia
[5] Electron Microscopy Unit, UNSW Sydney, Sydney, NSW 2052, Australia
[6] ARC Research Hub for Integrated Device for End-User Analysis at Low Levels, Faculty of Science, University of Technology Sydney, Sydney, NSW 2007, Australia
[7] UTS-SUStech Joint Research Centre for Biomedical Materials and Devices, Department of Biomedical Engineering, Southern University of Science and Technology, Shenzhen, Guangdong 518055, China

1 Introduction

It has been commonly accepted that tumorigenesis and cancer progression constitute a multistep process [1]. To date, the most commonly used method for cancer diagnosis and prognosis to guide treatment decisions is based on a complex combination of imaging and invasive tissue biopsies [2]. However, the methods are not always sensitive to early-stage cancer diagnosis and partially reflect the biology of tumour progression, due to intratumoral and intermetastatic genetic heterogeneity [3]. Small extracellular vesicles (sEVs) are nanometre-sized, bilayer lipid carriers, and contain a wide variety of cargos, including lipids, proteins, metabolites, RNAs and DNAs [4]. sEVs released from original cancer cells exist in almost all body fluids. They can become the potential circulating biomarkers in liquid biopsies, as they uniquely reflect the dynamic biological changes associated with the growing tumours and indicate the stages of a cancer progression [5, 6]. Optical characterizations of single sEV in high throughput will reveal the spatiotemporal dynamics and distributions of EVs to advance our knowledge in molecular biology [7]. However, considering their small sizes below the optical diffraction limit and complexities in carrying the various biomolecules, most methods based on optical microscopy are insufficient in resolving their nanoarchitectures and heterogeneity in cargo distributions [8].

Super-resolution microscopy techniques have emerged by pushing the resolution beyond the diffraction limit towards nanometre scales [9–13]. The most commonly used techniques include structured illumination microscopy (SIM), stimulated emission depletion (STED) microscopy, and single-molecule localization microscopy (SMLM) of stochastic optical reconstruction microscopy (STORM) and photoactivated localization microscopy (PALM) [14, 15]. SIM is a useful technique for fast-changing event within live-cell imaging studies, but the resolution of typically over 100 nm is insufficient in resolving the molecular information on sEVs. PALM using fluorescent protein Dendra2 and STORM using CellVue® Claret far-red fluorescent membrane dye have been applied to study the interactions of EVs with neurons in Alzheimer's disease with a localization precision of 25 nm achieved [16]. SMLM has been recently used to image quantum dot-labelled EVs with a spatial resolution of 30 nm achieved [17]. A new class of photoswitching polymer dots has been used to map of the surface proteins on sEVs [18]. SMLM, including PALM [19] and STORM [20, 21], offers high spatial resolution in the range of 20–50 nm, but are low throughput typically requiring several minutes for collection and reconstruction of multiple single molecule images.

STED, based on laser scanning microscopy, is powerful in providing both the sub-50 nm resolution and high imaging speed, but it requires two laser beams tightly aligned in a dedicated setup and the high excitation power density typically in the range of over 10^8 W/cm^2, which poses a major challenge in choosing fluorescence dyes and probes with both photo-stable and photoswitchable properties. Its higher optical resolution comes at the expense of more light exposures that induces major concerns in photobleaching and phototoxicity. To resolve single sEV, the efficient use of photon budget towards high contrast and the optimization of labelling specificity are further the challenging factors [15].

Lanthanide-doped upconversion nanoparticles (UCNPs) has been discovered with nonlinear photoswitchable properties, and suitable for STED-like superresolution nanoscopy with sub-30 nm optical resolution in resolving the cluster of single UCNPs [22]. It has been further demonstrated to imaging cytoskeleton structures [23], actin fibres [24], actin filaments [25] of Hela cells, sub-cellular structures of neuronal cells [26], and even deep tissues [27, 28]. Compared with the conventional dyes used in STED, a number of so-discovered new nonlinear optical properties can typically reduce the excitation power density by over three orders of magnitude, in the range of 10^5 W/cm^2. Other superior advantages using UCNPs in nanoscopy include: (1) their non-photobleaching and non-blinking properties, (2) the single-molecule sensitivity achieved by their intense brightness due to the high concentration of tens of thousands of lanthanide ions being doped within each nanocrystal, and (3) the negligible background level in detecting the anti-Stokes shift emissions under the near infrared excitation. Our recent work [29] using UCNPs further achieved the ultra-sensitivity in quantitative detection of sEVs, which recorded a limit of detection 1.8×10^6 EVs/mL, nearly 3 orders of magnitude lower than the standard enzymelinked immunosorbent assay (ELISA).

Here, we further improve the imaging resolution compared with our recent work, and present a strategy of UCNPs for super-resolution characterization the surface markers on single EVs (Fig. 1). The approach is based on the use of uniform, bright and photostable UCNPs, each highly doped with tens of thousands of lanthanide ions. EVs were firstly captured on a slide coated with CD9 antibody, targeted by the biotinylated epithelial cellular adhesion molecule (EpCAM) antibody, and subsequently labelled by streptavidin-UCNPs. The UCNPs on single sEVs were visualized via a STED-like super-resolution microscope, which is based on a single-beam scanning technique. When a single UCNP is in the middle of the doughnut beam, it generates a doughnut-shaped emission pattern with a dip at the position where the UCNP
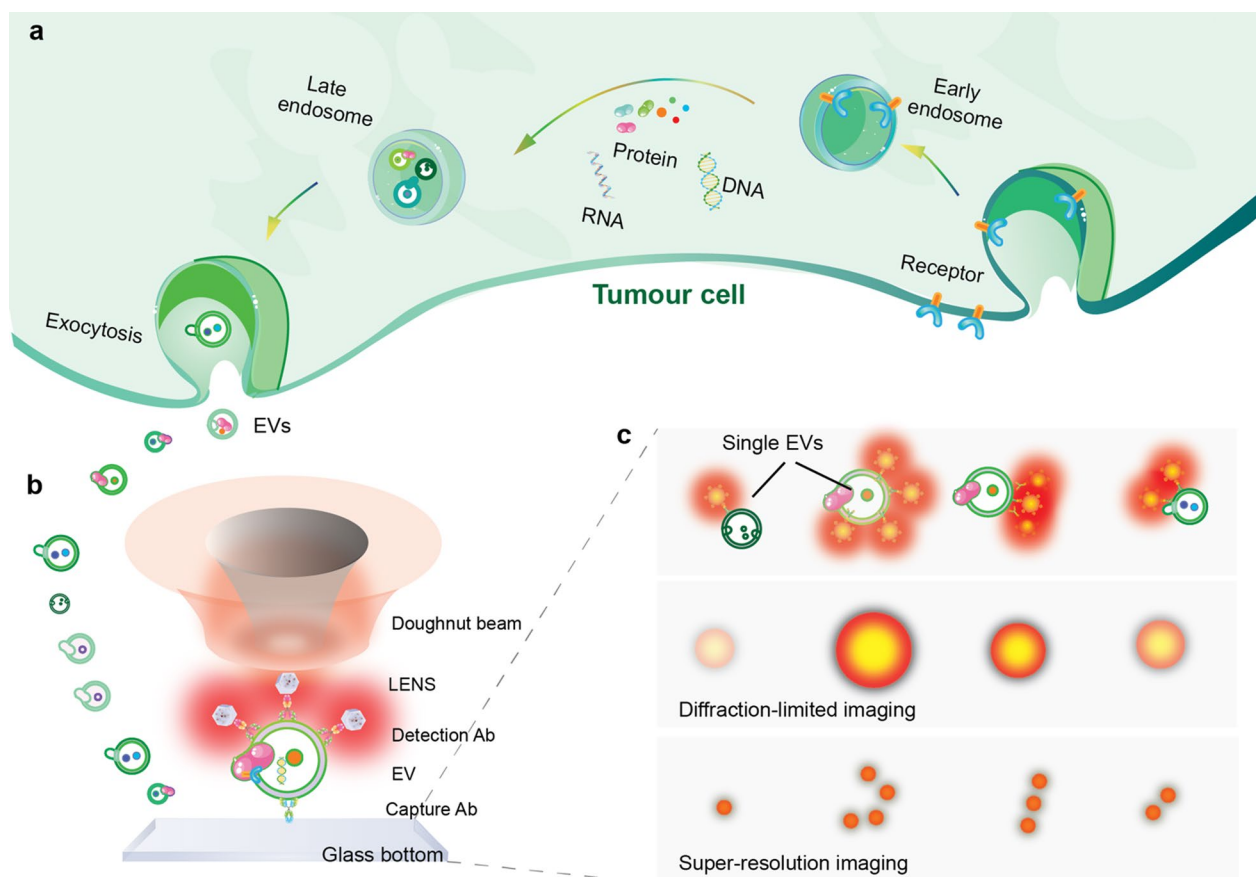
Fig. 1 Schematic illustration of upconversion nanoparticles (UCNPs) for the super-resolution quantification of surface biomarkers on single tumour cell-derived small EVs. **a** sEVs carrying heterogeneous distribution of biomarkers are released from the tumour cell. **b** sEVs can be captured on an antibody-coated plate and labelled by UCNPs. **c** UCNPs -EV conjugates detected as single bright spots with different intensities can be super-resolved in super-resolution nanoscopy

sits. The resolution is essentially determined by the emission power dependence curve of UCNPs and defined by a full-width at half-maximum (FWHM) of the dip at the measured point spread function (PSF) of a single UCNP [27, 30, 31].

We demonstrate that super resolution imaging of single sEVs can be achieved by the use of a library of UCNPs doped with different kinds and varied concentrations of emitters. We confirm that antibody conjugated UCNPs can specifically target tumour epitope EpCAMon both large EVs and single sEVs. Using super-resolution imaging, we can quantify the specific number of UCNPs on each EV, and theoretically analyse the size and steric hindrance of UCNPs on single sEVs.

2 Results
2.1 Optical performance evaluation of Er^{3+} and Tm^{3+} doped UCNPs
It has been demonstrated that a variety of lanthanide (Ln^{3+}) ions can be co-doped in nanocrystal host and

exhibit the photon upconversion process, which converts the low-energy photons in near infrared (NIR) into high-energy photons in the visible and ultraviolet (UV) range [32]. Among them, Er^{3+}, Tm^{3+} ions, with a ladder-like metastable energy level structure, are the commonly used activators (emitters) in UCNPs.

Here, we first investigate the effect of emitters on their optical performance using a purpose-built single donut-beam scanning super resolution nanoscopy (Additional file 1: Note S1 and Additional file 1: Fig. S1). We synthesized Er^{3+}-doped UCNPs (2 mol%; 39.9 nm $\pm$ 2.8 nm, Additional file 1: Fig. S2a) and Tm^{3+}-doped UCNPs (4 mol%, 39.3 $\pm$ 1.6 nm, Additional file 1: Fig. S2b). The similar size of Er^{3+}-doped UCNPs and Tm^{3+}-doped UCNPs allows us to directly compare their brightness of single UCNPs. When getting excited by 980 nm, the emission bands of Tm^{3+}-doped UCNPs are mainly centred at 450 nm, 475 nm, 650 nm, and 800 nm, the emission bands of Er^{3+}-doped UCNPs are mainly centred at 550 nm and 650 nm (Fig. 2a). Upconversion is a
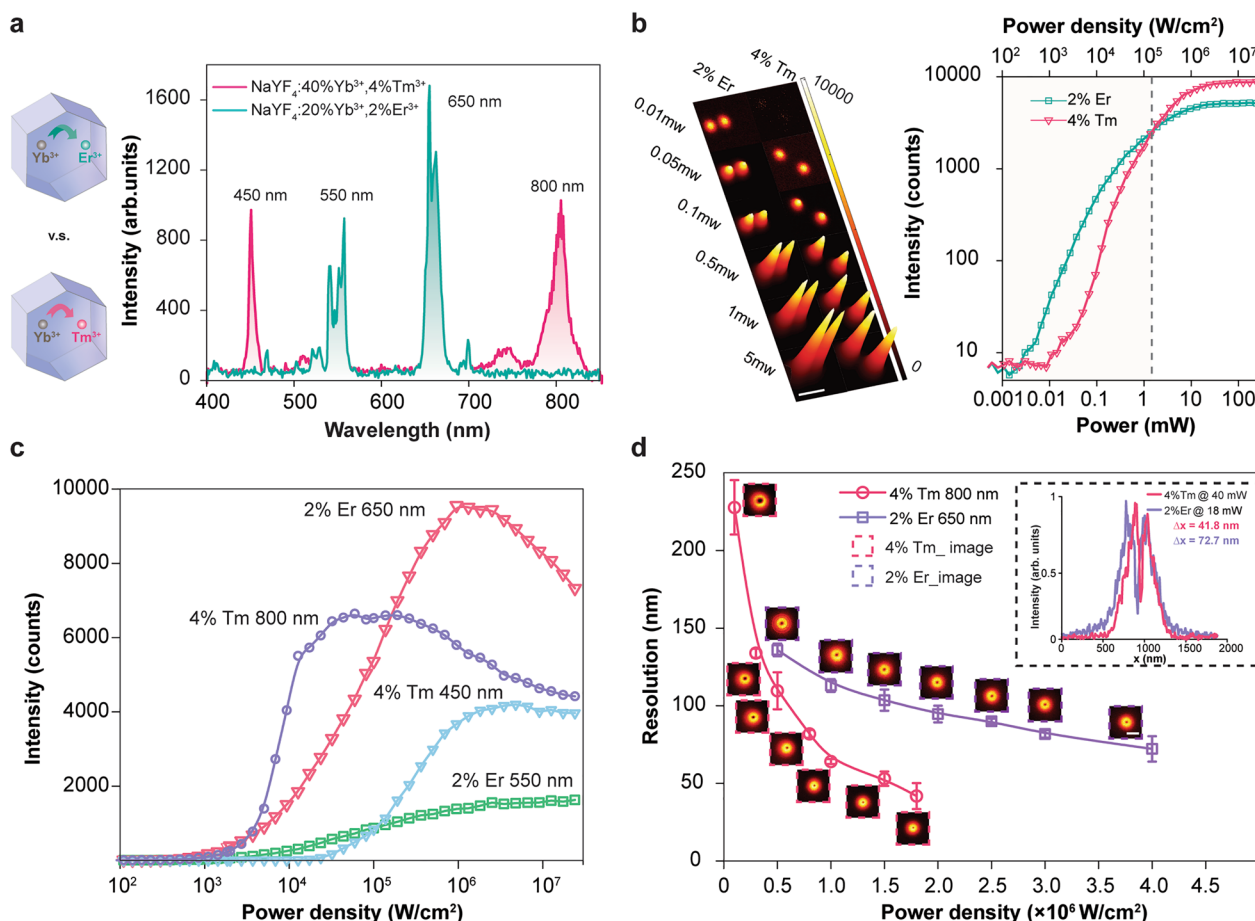
Fig. 2 The intensities and nonlinear properties of Er^{3+}-doped and Tm^{3+}-doped UCNPs. **a** The upconversion emission spectra of Er^{3+}-doped UCNPs and Tm^{3+}-doped UCNPs. **b** Left: Confocal images of Er^{3+}-doped UCNPs and Tm^{3+}-doped UCNPs under different excitation power. Right: Total power-dependent upconversion emission intensity obtained from single Er^{3+}-doped and Tm^{3+}-doped UCNPs. Scale bar: 1 μm. **c** Power-dependent upconversion emission intensity obtained from single Er^{3+}-doped UCNPs at 650 nm and 550 nm and single Tm^{3+}-doped UCNPs at 800 nm and 455 nm. **d** Super-resolution scaling Δx of UCNPs as a function of the excitation power (intensity). Inset, cross section profile lines of 4% Tm^{3+}-doped UCNPs at 1.8×10^6 W/cm^2 and 2% Er^{3+}-doped UCNPs at 4×10^6 W/cm^2. Error bars indicate standard deviations from line profiles of several measurements. Scale bar: 500 nm

multiphoton absorption process (Additional file 1: Fig. S3a), which is determined by the threshold of excitation power. Under the increased excitation power density from 10^2 W/cm^2 to 10^7 W/cm^2, the total brightness of single UCNPs is strongly power-dependent (Fig. 2b). We further investigated the relationship between the emission intensities of different emission bands and excitation power. The result shows that there is a linear fitting of log-log dependence between the upconversion intensity of emission band and laser excitation power (Additional file 1: Fig. S3b, c). The slope on a curve corresponds to the number of photons needed for the upconversion process. For Tm^{3+}-doped UCNPs, the slope of the 800 nm emission ($^3H_4$-$^3H_6$) is 1.4, indicating a two-photon transition. The slopes of the 475 nm ($^1G_4$-$^3H_6$) and

650 nm ($^1G_4$-$^3F_4$) emission both are 2.8, indicating a three-photon transition. The slope of the 450 nm emission ($^1D_2$-$^3F_4$) is 3.7, indicating a four-photon transition. For Er^{3+}-doped UCNPs, the slopes of the 550 nm ($^2H_{11/2}$/$^4S_{3/2}$-$^4I_{15/2}$) and 650 nm emission ($^4F_{9/2}$-$^4I_{15/2}$) are 1.6 and 1.5, respectively, indicating both are two-photon transition. Higher photon numbers require higher excitation power to excite the lower state into the higher state. When the laser power is relatively low, the intensity mainly comes from the two-photon transition. When the laser power is high enough, the intensity composition changes to three- or four-photon transitions. Therefore, Er^{3+}-doped UCNPs (mainly two-photon transition) is brighter than Tm^{3+}-doped UCNPs under low excitation power density (below 5×10^5 W/cm^2, Additional

file 1: Table S1), whereas Tm^{3+}-doped UCNPs (mainly three- or four-photon transition) becomes brighter than Er^{3+}-doped UCNPs under relatively high excitation power density.

We then compared the nonlinear properties of Er^{3+}-doped UCNPs and Tm^{3+}-doped UCNPs for super-resolution imaging. We selected emission peaks at 550 nm and 650 nm for Er^{3+}-doped UCNPs and emission peaks at 455 nm and 800 nm for Tm^{3+}-doped UCNPs. There are three features from the curve affecting the resolution: the power point (I_{Sat}) to achieve the half value of the maximum emission intensity, the power point (I_{STED}^{max}) to achieve the maximum emission intensity with fixed I_{Sat}, and the onset value of the curve (the power point to achieve e^{-2} of the maximum emission intensity). The resolution increases with lower I_{Sat} and I_{STED}^{max} and Larger onset value. For upconversion process, the visible output intensity (I) will be proportional to some power (n) of the excitation power,

$$I \propto I_{ex}^n$$

where n is the number of non-infrared radiation (NIR) photons absorbed per visible photon emitted. The smaller the slope (n) is, the lower I_{Sat} and I_{STED}^{max} are. According to the power-dependent upconversion luminescence intensity (Fig. 2c), For Er^{3+}-doped UCNPs, the slopes of the 550 nm and 650 nm emissions both are two-photon transition. But the population of 550 nm ($^2H_{11/2}/^4S_{3/2}$-$^4I_{15/2}$) located in the higher excited-state than 650 nm ($^4F_{9/2}$-$^4I_{15/2}$), exciting the population into the higher excited state of $^4F_{9/2}$ level must undergo much more non-radiative relaxation. So 650 nm emission has lower I_{sat} and I_{STED}^{max} than 550 nm emission. As for Tm^{3+}-doped UCNPs, 800 nm emission peak (two-photon transition) has lower I_{Sat} and I_{STED}^{max} compared with the emission at 455 nm, 475 nm and 650 nm (three/four-photon transition).

We further measured the FWHM of the dip at the measured PSF of UCNPs at various laser power density to define the experimental resolution (Additional file 1: Fig. S4). For 650 nm emission of Er^{3+}-doped UCNPs, the FWHM reduces slightly from 136 nm to 72.7 nm with the excitation power density increases from 5×10^5 W/cm^2 to 4×10^6 W/cm^2. Meanwhile, the FWHM of 800 nm emission from Tm^{3+}-doped UCNPs decrease significantly from 227 nm to 41.8 nm with the excitation power density increases from 1×10^5 W/cm^2 to 1.8×10^6 W/cm^2 (Fig. 2d). Moreover, Tm^{3+}-doped UCNPs (800 nm emission) have sharper curvature than Er^{3+}-doped UCNPs (650 nm) in the onset of the saturation curves and can quickly reach the saturated point with lower values of I_{Sat} and I_{STED}^{max}.

Therefore, Tm^{3+}-doped UCNPs is chosen in super-resolution imaging due to its better nonlinear response

performance and higher resolution than Er^{3+}-doped UCNPs.

2.2 Co-localization of EpCAM-mGFP EV with UCNPs to evaluate labelling specificity

As the sizes of nanoparticles and the likely aggregates of nanoparticles are in the same range of sEVs, the specific binding between EVs and UCNPs becomes essential in preventing the false positives in super-resolution characterization and quantification of single EV with UCNPs labeling. Er^{3+}-doped UCNPs was used in the specificity evaluation as it has brighter brightness under low power excitation. After two steps of surface modifications and characterisation, uniform and bright UCNPs are ready for the following experiments (Additional file 1: Figs. S5 and S6). To evaluate the specificity of UCNPs@P*b*P@SA, two groups of negative controls were assessed (Additional file 1: Fig. S7). The difference between the ability of UCNPs@P*b*P@SA (Mean = 5338) and UCNPs@P*b*P (Mean = 19) to recognize EVs is highly significant ($P < 0.0001$). The difference between the ability of UCNPs@P*b*P@SA to detect samples with EVs (Mean = 5338) or without EVs (Mean = 41) is highly significant ($P < 0.0001$). The results confirm the specificity of UCNPs@P*b*P@SA for detecting EVs.

To further ensure the specificity binding of UCNPs to the tumour epitope on single EV, we cross-validated the UCNPs labelled EVs by conducting a co-localization experiment between UCNPs and membrane-bound form of genetically encoded green fluorescent protein (mGFP) under 980 nm and 488 nm excitation, respectively (Fig. 3a). The co-localization characterization and wide-field imaging were conducted by the purpose-built optical setup (Additional file 1: Fig. S8).

Tumour epitope EpCAM is overexpressed in many human adenocarcinomas and squamous cell carcinomas [33]. We transiently expressed N-terminal GFP fusions of EpCAM oriented to the cytosolic side of in HT29 cells, thereby oriented to the cytosolic side of the EV membrane as an EV biomarker. To confirm the successful expression of EpCAM with mGFP tag in HT29 cells, the fluorescent signals of HT29 cells were detected at 24 h, 48 h and 72 h after transfection and the effective increase of signal intensity was observed in a 72-h period (Additional file 1: Fig. S9a). To further confirm the integration of EpCAM with mGFP tag into EV comportments, we isolated the small EVs, medium EVs and large EVs using differential centrifugations by 72-h post-transfection of cells. The expression of EpCAM-mGFP in EVs is validated by fluorescence imaging with EVs being detected as diffraction limited GFP fluorescent spots (Additional file 1: Fig. S9b).
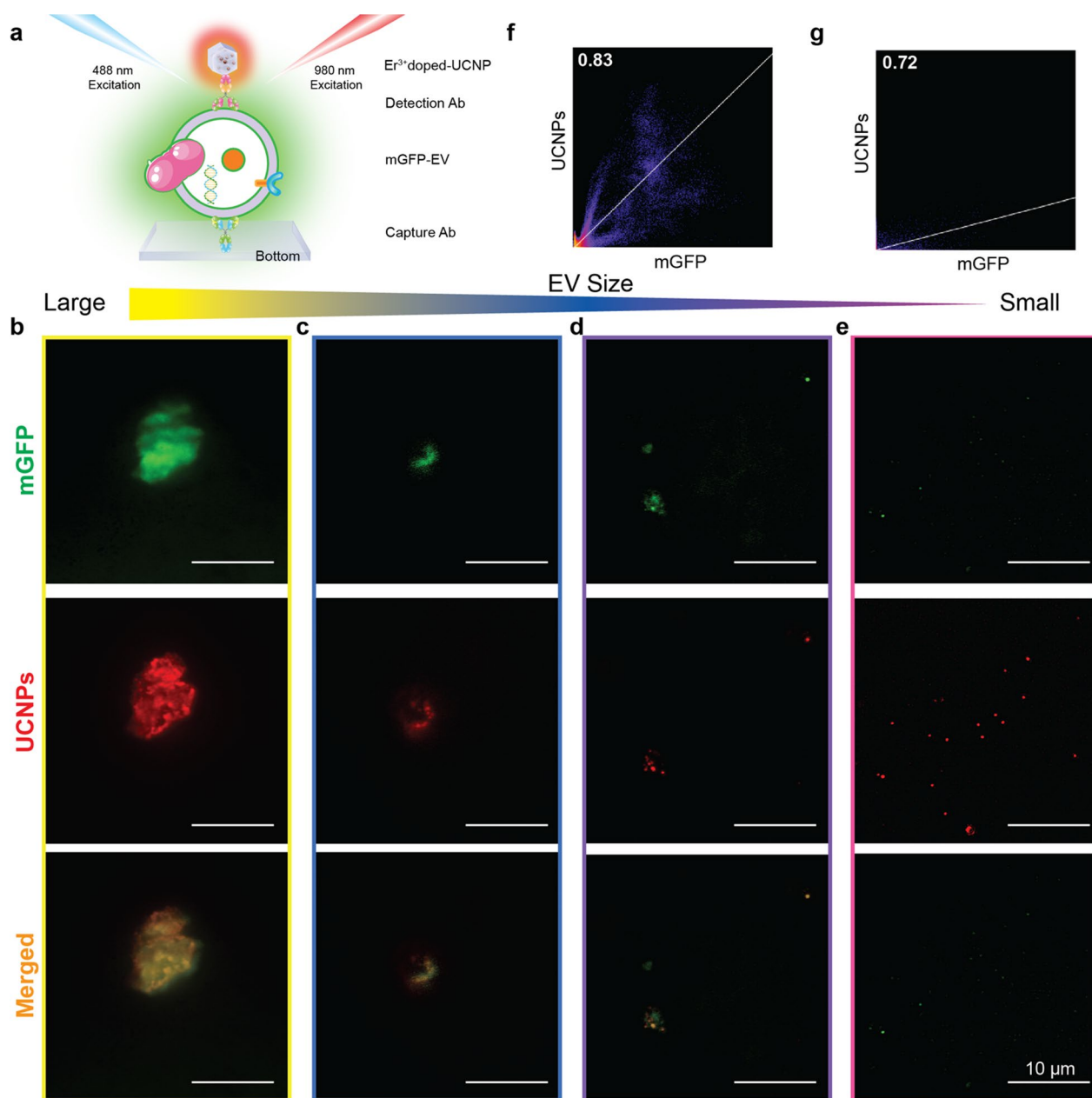
Fig. 3 Co-localization of the large, medium and small EpCAM-mGFP EVs specifically labelled by UCNPs**. a** Schematic illustration of co-localization experiment. **b**, **c**, **d**, mGFP/ UCNPs double labelled [EpCAM+]EVs with the sizes decreasing from large to small under the 488 nm and 980 nm excitation of a purpose-built wide-field fluorescence microscope, confirming a relatively high degree of co-localization. Scale bar, 10 μm. **f** Pearson's R analysis of mGFP-UCNPs co-localize for aggregated EVs (**b**). **g** Pearson's R analysis of mGFP-UCNPs co-localize for large EVs (**c**)

In our co-localization experiments between Er^{3+}-doped UCNPs and membrane-bound form of mGFP genetically modified EVs (Fig. 3a), the EpCAM-mGFP EVs were firstly captured by tetraspanin protein CD9, then detected as green fluorescent spots under 488 nm excitation, and subsequently labelled by Er^{3+}-doped UCNPs using biotinylated EpCAM antibody and detected as green fluorescent spots. It is

noteworthy that the mGFP emission and UCNPs emissions were completely orthogonal, e.g., mGFP green emission was invisible under 980 nm excitation and the UCNPs green and red emissions were silent under 488 nm excitation. To differentiate mGFP from UCNPs in colocalization experiments, we use pseudocolour of red to represent UCNPs image spots.

Pearson's Correlation Coefficient is a commonly accepted method used to quantify the degree of colocalization between fluorophores [34]. It is a value computed to be between -1 (perfect negative correlation) and 1 (perfect positive correlation), while 0 means that there is no correlation. For large EVs and EV aggregates, shown in Fig. 3b, c, Pearson's R-values of 0.83 and 0.72 were recorded, respectively (Fig. 3f, g), indicating that Er^{3+}-doped UCNPs-labelled EVs had strong co-localization with EpCAM-mGFP EVs. However, for medium EVs and small EVs (Fig. 3d, e), Pearson's R-values of only 0.31 and 0.20 were achieved, respectively (Additional file 1: Fig. S10). We observed that small and medium sized mGFP spots under 488 nm excitation can be barely detected against the strong auto-fluorescent background, which requires post-processing (deconvolution) to remove the background without certainty. The uncertainty was further affected by the fast photo-bleached fluorescent signals from small and medium sized mGFP spots. Small mGFP spot has faster photo-bleaching time and higher auto-fluorescent background compared with UCNPs, which requires post-processing (deconvolution) to remove the background and smoothen the signal. Pearson's R-value is therefore not suitable for evaluating the co-localization efficiency for sEVs due to the many artefacts.

We then chose to count the number of overlapped spots after deconvolution (the number of overlapped spots between UCNPs and mGPF over total spots). A population of double-positive spots confirmed a certain degree of fluorophore co-localization (∼65%, for Fig. 3e). Taking together all the above analysis, we conclude that UCNPs labelling was rather specific, sufficiently bright, and photo-stable for long-term and quantitative analysis of single sEVs.

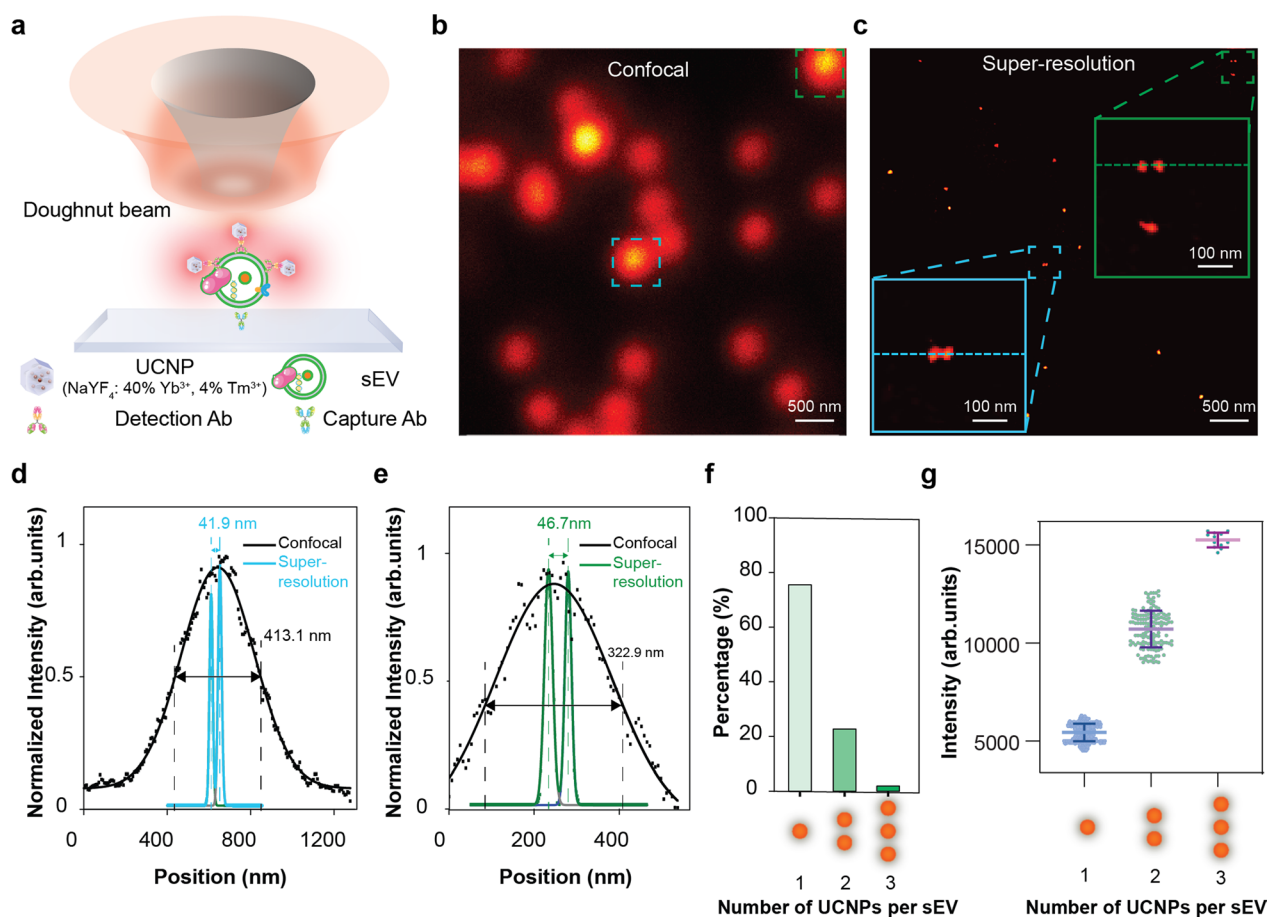## 2.3 Single sEV characterization by super-resolution microscope

To ensure most of the isolated particles are sEVs, we first conducted cryo-EM characterization which shows the lipid bilayers structures of the isolated sEVs (Additional file 1: Fig. S11a). The cryo-EM images also indicate the heterogeneous size and morphology of sEVs. The nanoparticle tracking analysis results (Additional file 1: Fig. S11b) present the modal size of the obtained HT29-derived sEVs is around 143.6 ± 3.3 nm. More than 72% of particles were below 200 nm, which is the definition range of sEVs [35]. Western blotting analysis shows the presence of tetraspanin marker CD9. The absence of non-sEV marker calnexin confirms that there were no other large EVs in the sample. In addition, the expression of EpCAM is observed in HT29 cells-derived sEVs (Additional file 1: Fig. S11c).

Tm^{3+}-doped UCNPs are bright, highly uniform and resist to photobleaching after surface modification (Additional file 1: Figs. S12 and S13). To quantify the exact number of UCNPs per localization cluster, we employ a tightly focused doughnut-shaped excitation beam to scan across a sample (Fig. 4a). During the scanning, when a single UCNP is placed in the middle of the doughnut profile, it comes across minimized excitation power, thereby generating a doughnut-shaped emission pattern with a dip at the position where the UCNPs sits. To demonstrate the super-resolution utility of UCNPs, Fig. 4b shows two typical areas of sEV clusters (in blue and green) in a confocal image, which does not provide sufficient resolution to tell the number or position of UCNPs on single EVs. In contrast, the super-resolution image clearly resolves single UCNPs from the clusters (Fig. 4c), e.g. UCNPs separated by 41.9 nm and 46.7 nm, respectively in Fig. 4d and e.

With this super-resolution capability, we can resolve the populations of single EVs by the specific number of UCNPs (More representative images are shown in Additional file 1: Fig. S14). For instance, in a single testing sample isolated from HT29 cells, percentage of singly, dually, triple UCNPs on a per vesicle basis for the expression of EpCAM are 75.5%, 22.6% and 1.9%, respectively (Fig. 4f). As the intensity of our UCNPs are intensity uniform, the super-resolved results can be further validated by the intensity of bright signal spots on the number of UCNPs per sEV, which shows the luminescence intensities of triplet and doublet UCNPs are three times and twice that of single UCNPs (Fig. 4g).

2.4 The size limitation and theoretical labelling density

Figure 5 illustrates the size limitation of UCNPs for resolving the epitopes of a single sEV. The size of synthetic inorganic nanoparticles approaches the size of small EVs, therefore the high labelling density becomes critical for super resolution microscopy to image the envelope of sEVs with a resolution of a few tens of nanometers. However, to produce high brightness, the majority of currently developed nanoparticles are relatively large (around 20–50 nm) [36]. To illustrate how the size of UCNPs affects the maximum number of UCNPs being used for single sEV labelling, we first calculated the optimized number of UCNPs that can be densely packed on the surface of sEV, assuming epitopes are sufficiently high, compared with the number of UCNPs. As illustrated in Fig. 5a and Additional file 1: Note S10, one can expect the use of smaller UCNPs with minimal length of the surface functional groups and small hydrodynamic diameters to reduce the steric hindrance effect on labelling multiple UCNPs on single sEVs.

Fig. 4 Super-resolution characterization of single sEVs by UCNPs labelling. **a** Schematic illustration of scanning a doughnut excitation beam to resolve UCNPs clusters on single sEVs. **b** Confocal microscopic image of UCNPs clusters. **c** Super-resolution image of the same UCNPs clusters as those in (**b**). Blue and green dashed boxes mark an area containing multiple adjacent UCNPs that can be resolved in super-resolution microscopy, but not in confocal imaging. **d**, **e** Line profiles of the UCNPs clusters from the confocal image and super-resolution image. Two clusters of doublet UCNPs can be resolved with the UCNPs particles separated by 41.9 nm and 46.7 nm, respectively. Pixel dwelling time: 1 ms. Scanning step size: 10 nm. **f** The percentage of the number of UCNPs per sEV resolved and quantified by super-resolution imaging in a single testing sample. There are 75.47% of singlet UCNPs, 22.64% of doublet UCNPs, and 1.89% of triplet UCNPs on single sEVs. $n=100$. **g** The averaged luminescent intensity of bright signal spots on the number of UCNPs per single sEV ($n=100$), showing the three populations of single EVs carrying one, two, or three UCNPs

To reach the size limitation, we synthesised Tm^{3+}-doped UCNPs (6 mol%) with the sizes of 18.1 nm (± 0.9 nm) and 27.3 nm (± 1.2 nm) (Additional file 1: Fig. S15). Same as 40 nm UCNPs, EVs (concentration: 9.6×10^7 vesicles/mL) were captured on a slide coated with CD9 antibody, targeted by the biotinylated EpCAM antibody, and subsequently labelled by streptavidin-UCNPs (18 nm or 27 nm separately). At the single vesicle level, we observed the UCNPs on single vesicles using super-resolution microscopy and found that the number of UCNPs are heterogenous on each single vesicles. As the intensity of each single sEV spot labelled by UCNPs is proportional to the number of UCNPs (Additional file 1: Fig. S16), we analysed 241 vesicles labelled by 27 nm UCNPs, and found that the number of UCNPs labelled

on single vesicle is ranging from 0 to 9. We also analysed 144 vesicles labelled by 18 nm UCNPs, and found that the number of UCNPs labelled on single vesicle is ranging from 0 to 21. This is coherent with theoretical calculation that smaller size will reduce steric hindrance effect – experimental maximum UNCP could labelled on single vesicles is increased from 3 to 9 and 21 (Fig. 5c). Moreover, we calculated the proportions of different numbers of UCNPs on single vesicles, and found that sEVs were highly heterogeneous with various sizes and morphology observed by cryo-electron microscopy (Fig. 5b), suggesting the subpopulations of EVs [37, 38].

Several reasons account for the differences among the various numbers: the different quantity of the surface biomarkers even when EVs have same size, the sizes of
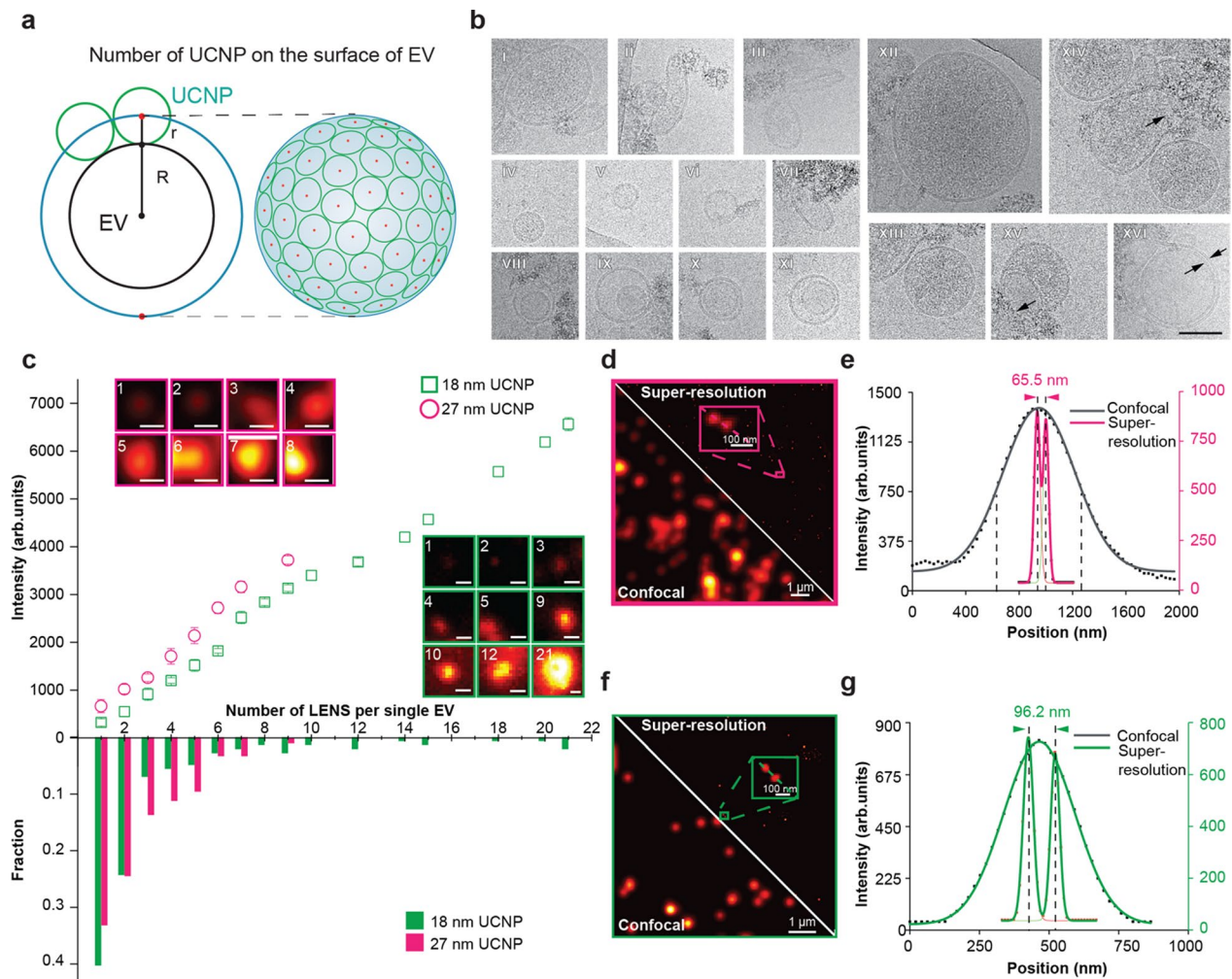
Fig. 5 The heterogeneity of sEVs and size limitation of UCNPs. **a** the theoretical number of UCNPs that can be labelled on the surface of an EV limited by the size of UCNPs. **b** Cryo-EM images of heterogenous sEVs isolated from HT29 cells. i-vii, single vesicles with heterogeneous size and morphology; viii-xi, double vesicles; xii-xiii, vesicles with electron-dense cargo in lumen; xiv-xv, vesicles with broken membrane (point with black arrow); xvi, double-membrane vesicles. Scale bar: 100 nm. **c** Positive Y axis: The measured intensity profiles along the increasing number of UCNPs per single EVs. Error bars: ± s.d. Insets: representative single diffraction-limited spots with the intensity correlated to the number of UCNPs per spot. Negative Y axis: Statistical distribution of the measured intensity profiles over the $N_{27nm} = 241$ and $N_{18nm} = 144$ counted spots, respectively. **d** Comparison between the confocal image and super-resolution image of the same area using 27 nm UCNPs. Pink box: zoom in view of the dashed pink box. Pixel dwelling time: 4 ms. Scanning step size: 10 nm. **e** Cross-sectional profiles of two adjacent UCNPs correspondence to the boxed region in **d**. **f** Comparison of confocal imaging and super-resolution imaging of the same area using 21 nm UCNPs. Green box: zoom in view of the dashed green box. Pixel dwelling time: 5 ms. Scanning step size: 10 nm. **g** Cross-sectional profiles of two adjacent UCNPs correspondence to the boxed region in **f**

the EVs, both sizes and epitopes are different. For example, large number of UCNPs could come from small EVs have large number of epitopes of EpCAM. Small number of UCNPs could also come from larger EVs have a few number of epitopes. This the magical and difficulty of studying EVs, their physical characteristics (size, density, morphology) and cargos (protein, lipid content, nucleic acids) are heterogeneous even when they are from a same parental cell. No matter what kind of reasons, it is the heterogeneity beneath the CD9 + vesicles subpopulation.

The super-resolution images show the enhanced resolution to confirm the intensity counting results, e.g. Figure 5d shows a typical area of 27 nm UCNPs clusters (in pink) clearly resolved by super-resolution image, separated by 65.5 nm (Fig. 5e); Fig. 5f shows a typical area of unresolvable clusters by confocal imaging (in green) clearly resolved by super-resolution image using 18 nm UCNPs, separated by 96.2 nm (Fig. 5g). Theoretically, the smaller particle size will induce a smaller value of the FWHM, which offers a higher resolution. However, the

final experiment PSF is not only affected by the spatial profile, but also by the intensity of UCNPs. The intensity will loss when functionalize UCNPs from hydrophobic state to hydrophilic state. The mean intensities of 18-nm, 27-nm and 40-nm UCNPs after surface modification are 311, 480, and 5427, respectively (Additional file 1: Fig. S17). When the size of UCNPs is too small, their low intensity plus loss of the intensity lead to a low signal-to-noise ratio, thereby resulting in a lower resolution of experimentally PSF. Therefore, we found the highest resolution was not achieved for the smallest nanoparticles.

3 Discussion and conclusion

Circulating EVs in the bodily fluids are promising biomarkers for tumour diagnosis, prognosis, prediction, and treatment response assessment. EVs are inherently heterogenous and featured with varied sizes, morphologies and compositions of cargos [8]. Compared with fluorescence microscopy, the super-resolution approach presented here achieves a sub-50 nm imaging resolution for single sEV characterization, allowing for the visualization of individual EVs and the identification of surface-marker subpopulations of heterogeneous EVs. Though the UCNPs is relatively large and cannot tell the absolute number of antigens on single vesicle, our method provides a way to quantify the changes of surface antigens on single EVs. Previously reported works demonstrated that EVs are inherently heterogenous and featured with varied physical characteristics (size, density, morphology) and cargos (protein, lipid content, nucleic acids) [8]. The sizes of isolated sEVs used in this paper are consistent along with the experiments and confirmed by the nanoparticle tracking analysis (NTA), ensuring that most of the isolated particles (72%) were below 200 nm which is in the definition of sEVs. Among all the vesicles, their sizes are heterogeneous. From Fig. 5d, we can see that the maximum number of UCNPs labelled on single vesicles are 21, whereas the minimum number of UCNPs labelled on single vesicle is 1. This is the heterogeneity beneath the CD9+ vesicles subpopulation.

It can be further used to monitoring EV heterogeneity changes along with the tumour progression progress. We have to admit that due to the size limitation of UCNPs, the number of UCNPs on single vesicles is not equal to the absolute number of epitopes. Compared with a previous report that there were up to ca 40–60 GFP-tagged tetraspanins per fluorescent sEV (size ca 80–120 nm) [13], our results using 18-nm UCNPs can label up to 21 EpCAM per vesicle, which could be used for reflecting the trend of proportion changes if not the absolute counts. The reason why EVs is attractive in the field of cancer research is that cancer-derived EVs can uniquely

reflect heterogeneous biological changes associated with growing tumors [7]. In contrast to the invasive tumour biopsy for histopathological analysis, liquid biopsy of EVs is readily accessible from nearly all body fluids, showing promise for early-stage diagnosis, prognosis, and surveillance of cancer [8]. Here, we can't exactly tell the reason where the heterogeneity come from. But one of important application of our approach is to apply our technology for clinical samples, such as blood samples from a continuously cancer progression patient. When, the proportions of UCNPs is comparable between different timepoints. Assuming there is a cancer patient, we set all the experimental parameter are the same exclude the time point of tumour progression, we collect his/her blood at different timepoint, the proportions of UCNPs between different timepoints can tell the progression or treatment. E.g. after drug treatment, the proportion of heavily expressed Epcam (21 number of UCNPs on single vesicles) are decreased from 50 to 30%, which may indicate that the drug treatment is effective.

The quality of this work can be improved by using the TEM and AFM to directly confirm the bioconjugation. However, in our case, the EVs/UCNPs are fixed on the surface of the plate (functionalized plate), which cannot take out to drop on the grid. The only way to realize TEM/AFM imaging after reaction is to conduct the reaction on the grid of TEM/AFM (cryo-EM is better, as EVs is biological sample), which needs the additional functionalization of the grid surface (not the way consistent with our whole experiments). But the transfection method used here is also a popular way for validating the specificity.

There are also limitations worth discussions. Successful isolation of EVs is also important. Here we chose the widely used method—PEG precipitation [39] to minimize the structural damage to the membrane of EVs with high yield and time saving compared with ultracentrifugation, but PEG may cause EVs' aggregation. We therefore checked the morphology and size of sEVs using NTA and cryo-EM and add additional step by tetraspanin antibody selection. Specific labelling is imperative for downstream analysis of EV surface subpopulations, which requires the specificity of a particular antibody that can recognize epitope. Compared with conventional probes, super-resolution microscopy approach using UCNPs suggests new scopes in pushing down the size of nanoparticles to gain the high labelling density as well as multiple emission colours and lifetimes of nanoparticles [40] to target a panel of orthogonal biomarkers [41]. Future experiments should also focus on improving the surface properties of UCNPs

and bioactivities of antibody conjugates as well as the target accessibility and the optimum distance between UCNPs and sEV, to improve the labelling efficiency of UCNPs towards diagnostic applications of clinical samples and monitoring the stages of tumour growth and cancer metastasis.

Supplementary Information

The online version contains supplementary material available at https://doi.org/10.1186/s43593-022-00031-1.

Additional file 1: Note S1. Super-resolution microscope setup. **Figure S1**. Optical setup of the super-resolution microscope. **Note S2.** UCNPs for optical performance evaluation. **Figure S2.** TEM images and size distribution histograms of the synthesized. **Figure S3.** The saturation profile of UCNPs. **Table 1.** The upconversion emission intensities obtained from single Er^{3+}-doped and Tm^{3+}-doped UCNPs under different excitation power (below 5 mW) in Fig. 2b. **Figure S4.** Emission intensity profiles of single UCNP at different laser powers. **Note S3.** UCNPs preparation and characterization. **Figure S5.** Preparation and characterization of UCNPs@ P*b*P@ SA. **Figure S6.** Properties of Er^{3+}-doped UCNPs@ P*b*P@SA after two-steps' surface modification used in Fig. 3. **Figure S7.** Evaluation of the specificity of the UCNPs@P*b*P@SA. **Note S4.** The optical setup for co-localization imaging. **Figure S8.** The optical layout of the co-localization microscope used in this work. **NoteS5.** EpCAM-mGFP tagged EV production and characterization. **Figure S9.** Cell transfection by plasmid. **Note S6.** mGFP-UCNPs co-localization. **Figure S10.** Pearson's R analysis of mGFP-UCNPs co-localize for medium EVs and sEVs. **Note S7.** sEV production and characterization for super resolution imaging. **Figure S11.** Characterisation of isolated EVs. **Note S8.** Tm^{3+}-doped UCNPs@P*b*P@SA preparation and characterisation. **Figure S12.** Tm^{3+}-doped UCNPs@P*b*P@SA after surface modification used in Fig. 4. **Figure S13.** The time series of upconversion confocal images recorded from the same area under continuous laser scanning excitation. **Note S9.** Super-resolution imaging of sEVs. **Figure S14.** Representative confocal microscopic image and its Super-resolution image of the same area. **Note S10.** Theoretical labelling density for UCNPs to label sEVs. **Note S11.** Tm^{3+}-doped UCNPs@P*b*P@SA preparation and characterisation for size limitation analysis. **Figure S15.** TEM images and size distribution histograms of the $NaYF_4$:20%Yb^{3+},6%Tm^{3+} nanoparticles. **Figure S16.** Confocal images of single particles and their intensities. **Figure S17.** Comparison of the mean intersities of 18-nm, 27-nm and 40-nm UCNPs@P*b*P@SA.

Author contributions

DJ and GH conceived the project. DJ supervised the project. GH conducted the experiments, prepared the figures, and wrote the manuscript. YL set up the optical system and conducted the optical characterization. SW synthesised the nanoparticles. DW supported cell transfection experiments. YZ and JR supported EV characterization experiments. All authors read and approved the final manuscript.

Declarations

Competing interests
Dayong Jin serves as an Editor for the journal, no other author has reported any competing interests.

References
1. G. Bergers, S.-M. Fendt, Nat. Rev. Cancer **21**, 162–180 (2021)
2. Editorial, Nat. Biomed. Eng. **1**, 925 (2017)
3. L.R. Yates, M. Gerstung, S. Knappskog, C. Desmedt, G. Gundem, P. Van Loo, T. Aas, L.B. Alexandrov, H. Davies, Y. Li, Y.S. Ju, M. Ramakrishna, H.K. Haugland, P.K. Lilleng, S. Nik-Zainal, S. McLaren, A. Butler, S. Martin, D. Glodzik, A. Menzies, K. Raine, J. Hinton, D. Jones, L.J. Mudie, B. Jiang, D. Vincent, A. Greene-Colozzi, P.-Y. Adnet, A. Fatima, M. Maetens, M. Ignatiadis, M.R. Stratton, C. Sotiriou, A.L. Richardson, P.E. Lønning, D.C. Wedge, P.J. Campbell, Nat. Med. **21**, 751–759 (2015)
4. M. Tkach, C. Théry, Cell **164**, 1226–1232 (2016)
5. A. Möller, R.J. Lobb, Nat. Rev. Cancer **20**, 697–709 (2020)
6. R. Xu, A. Rai, M. Chen, W. Suwakulsiri, D.W. Greening, R.J. Simpson, Nat. Rev. Clin. Oncol. **15**, 617–638 (2018)
7. S.T.-Y. Chuo, J.C.-Y. Chien, C.P.-K. Lai, J. Biomed. Sci. **25**, 91 (2018)
8. G. Huang, G. Lin, Y. Zhu, W. Duan, D. Jin, Lab. Chip. **20**, 2423–2437 (2020)
9. Z. Nizamudeen, R. Markus, R. Lodge, C. Parmenter, M. Platt, L. Chakrabarti, V. Sottile, Biochim. Biophys. Acta. Mol. Cell Res. **2018**, 1891–1900 (1865)
10. C. Han, H. Kang, J. Yi, M. Kang, H. Lee, Y. Kwon, J. Jung, J. Lee, J. Park, J. Extracell. Vesicles **10**, e12047 (2021)
11. R.R. Iyer, J.E. Sorrells, L. Yang, E.J. Chaney, D.R. Spillman, B.E. Tibble, C.A. Renteria, H. Tu, M. Žuraukas, M. Marjanovic, S.A. Boppart, Sci. Rep. **12**, 3438 (2022)
12. K. Burbidge, V. Zwikelmaier, B. Cook, M.M. Long, B. Balva, M. Lonigro, G. Ispas, D.J. Rademacher, E.M. Campbell, J. Extracell, Vesicles **9**, 1789326 (2020)
13. G. Corso, W. Heusermann, D. Trojer, A. Görgens, E. Steib, J. Voshol, A. Graff, C. Genoud, Y. Lee, J. Hean, J.Z. Nordin, O.P.B. Wiklander, S. El Andaloussi, N. Meisner-Kober, J. Extracell. Vesicles **8**, 1663043 (2019)
14. G. Bordanaba-Florit, F. Royo, S.G. Kruglik, J.M. Falcón-Pérez, Nat. Protoc. **16**, 3163–3185 (2021)
15. L. Schermelleh, A. Ferrand, T. Huser, C. Eggeling, M. Sauer, O. Biehlmaier, G.P.C. Drummen, Nat. Cell Biol. **21**, 72–84 (2019)
16. J.C. Polanco, C. Li, N. Durisic, R. Sullivan, J. Götz, Acta Neuropathol. Commun. **6**, 10 (2018)
17. S. Zong, J. Zong, C. Chen, X. Jiang, Y. Zhang, Z. Wang, Y. Cui, Nanotechnology **29**, 65705 (2018)
18. Y. Jiang, L.A. Andronico, S.-R. Jung, H. Chen, B. Fujimoto, L. Vojtech, D.T. Chiu, Angew. Chemie Int. Ed. **60**, 13470–13475 (2021)
19. C. Chen, S. Zong, Z. Wang, J. Lu, D. Zhu, Y. Zhang, Y. Cui, A.C.S. Appl. Mater. Interfaces **8**, 25825–25833 (2016)
20. R.P. McNamara, Y. Zhou, A.B. Eason, J.T. Landis, M.G. Chambers, S. Willcox, T.A. Peterson, B. Schouest, N.J. Maness, A.G. MacLean, L.M. Costantini, J.D. Griffith, D.P. Dittmer, J. Extracell, Vesicles **11**, e12191 (2022)
21. Z. Nizamudeen, R. Markus, R. Lodge, C. Parmenter, M. Platt, L. Chakrabarti, V. Sottile, Biochim. Biophys. Acta. Mol. cell Res. **2018**, 1891–1900 (1865)
22. Y. Liu, Y. Lu, X. Yang, X. Zheng, S. Wen, F. Wang, X. Vidal, J. Zhao, D. Liu, Z. Zhou, C. Ma, J. Zhou, J.A. Piper, P. Xi, D. Jin, Nature **543**, 229–233 (2017)
23. Q. Zhan, H. Liu, B. Wang, Q. Wu, R. Pu, C. Zhou, B. Huang, X. Peng, H. Ågren, S. He, Nat. Commun. **8**, 1058 (2017)
24. Y. Liang, Z. Zhu, S. Qiao, X. Guo, R. Pu, H. Tang, H. Liu, H. Dong, T. Peng, L.-D. Sun, J. Widengren, Q. Zhan, Nat. Nanotechnol. **17**, 524–530 (2022)
25. X. Guo, R. Pu, Z. Zhu, S. Qiao, Y. Liang, B. Huang, H. Liu, L. Labrador-Páez, U. Kostiv, P. Zhao, Q. Wu, J. Widengren, Q. Zhan, Nat. Commun. **13**, 2843 (2022)

26. D. Denkova, M. Ploschner, M. Das, L.M. Parker, X. Zheng, Y. Lu, A. Orth, N.H. Packer, J.A. Piper, Nat. Commun. **10**, 3695 (2019)
27. C. Chen, F. Wang, S. Wen, Q.P. Su, M.C.L. Wu, Y. Liu, B. Wang, D. Li, X. Shan, M. Kianinia, I. Aharonovich, M. Toth, S.P. Jackson, P. Xi, D. Jin, Nat. Commun. **9**, 3290 (2018)
28. L. Liang, Z. Feng, Q. Zhang, T. Do Cong, Y. Wang, X. Qin, Z. Yi, M.J.Y. Ang, L. Zhou, H. Feng, B. Xing, M. Gu, X. Li, X. Liu, Nat. Nanotechnol. **16**, 975–980 (2021)
29. G. Huang, Y. Zhu, S. Wen, H. Mei, Y. Liu, D. Wang, M. Maddahfar, Q.P. Su, G. Lin, Y. Chen, D. Jin, Nano Lett. **22**, 3761–3769 (2022)
30. S.W. Hell, Nat. Biotechnol. **21**, 1347–1355 (2003)
31. G. Zhao, C. Kuang, Z. Ding, X. Liu, Opt. Express **24**, 23596–23609 (2016)
32. Q. Su, H.-L. Wei, Y. Liu, C. Chen, M. Guan, S. Wang, Y. Su, H. Wang, Z. Chen, D. Jin, Nat. Commun. **12**, 4367 (2021)
33. P. Amrollahi, M. Rodrigues, C. J. Rodrigues, A. Goel, H. Han and T. Y. Hu, Front. Genet. **10**, 1273 (2019)
34. E.M.M. Manders, F.J. Verbeek, J.A. Aten, J. Microsc. **169**, 375–382 (1993)
35. C. Théry, K.W. Witwer, E. Aikawa, E. Alcaraz, J. Extracell, Vesicles **7**, 1535750 (2018)
36. S. Wen, J. Zhou, K. Zheng, A. Bednarkiewicz, X. Liu, D. Jin, Nat. Commun. **9**, 2415 (2018)
37. A. Emelyanov, T. Shtam, R. Kamyshinsky, L. Garaeva, N. Verlov, I. Miliukhina, A. Kudrevatykh, G. Gavrilov, Y. Zabrodskaya, S. Pchelina, A. Konevega, PLoS ONE **15**, e0227949 (2020)
38. D. Zabeo, A. Cvjetkovic, C. Lässer, M. Schorb, J. Lötvall, J.L. Höög, J. Extracell, Vesicles **6**, 1329476 (2017)
39. Z. Andreu, E. Rivas, A. Sanguino-Pascual, A. Lamana, M. Marazuela, I. González-Alvaro, F. Sánchez-Madrid, H. de la Fuente, M. Yáñez-Mó, J. Extracell. Vesicles **5**, 31655 (2016)
40. D.J. Gargas, E.M. Chan, A.D. Ostrowski, S. Aloni, M.V.P. Altoe, E.S. Barnard, B. Sanii, J.J. Urban, D.J. Milliron, B.E. Cohen, P.J. Schuck, Nat. Nanotechnol. **9**, 300–305 (2014)
41. C. Liu, J. Zhao, F. Tian, L. Cai, W. Zhang, Q. Feng, J. Chang, F. Wan, Y. Yang, B. Dai, Y. Cong, B. Ding, J. Sun, W. Tan, Nat. Biomed. Eng. **3**, 183–193 (2019)